Journal of Materials Chemistry A

ROYAL SOCIETY OF CHEMISTRY

PAPER

View Article Online
View Journal

Cite this: DOI: 10.1039/d6ta01398h

Mitigating Ni migration in solid oxide electrolysis by altering Ni-YSZ electrode composition

Pattiya Pibulchinda,[a] Hugo Duchêne,[b] Bartlomiej Winiarski,[c] Maxime Hubert,[b] Peter W. Voorhees,[a] Katsuyo Thornton,[d] Jérôme Laurencin[b] and Scott A. Barnett*[a]

Nickel migration in nickel-yttria stabilized zirconia (Ni-YSZ) fuel electrodes is a significant degradation mechanism limiting the lifetime of solid oxide electrolysis cells, but the factors that control Ni migration are not well understood. Here, we demonstrate that the Ni/YSZ ratio plays an important role in Ni migration. Ni distribution was compared before and after electrolysis operation in 85% H_2O – 15% H_2, 800 °C, −1 A cm^{-2} for 500 hours. After testing, clear Ni depletion was observed near the electrolyte in the electrode with an initial 70 wt% NiO content (~38 vol% Ni, 35 vol% YSZ, 27 vol% pore in the reduced electrode), whereas no Ni depletion was observed in the electrode with an initial 50 wt% NiO content (~26 vol% Ni, 57 vol% YSZ, 17 vol% pore in the reduced electrode). Two mechanisms are proposed to explain this effect. First, the lower Ni content electrode exhibited ~45% lower polarization resistance (0.30 *vs.* 0.54 Ω cm^2 at 800 °C), reducing the overpotential driving force for migration. Second, 3D microstructural reconstruction revealed that the low-Ni electrode possessed substantially smaller and more isolated surface area per unit volume of Ni-pore interfaces (average *z*-length 0.97 μm *vs.* 2.43 μm), which limited the ability of Ni to migrate *via* surface diffusion across appreciable distances. These findings provide clear design principles for improving SOEC durability through composition optimization.

Received 13th February 2026
Accepted 1st June 2026

DOI: 10.1039/d6ta01398h

rsc.li/materials-a

Introduction

Electrolytic hydrogen plays a key role in plans to achieve net-zero emissions by storing intermittent renewable energy and producing renewable fuels for difficult-to-electrify sectors.[1] Amongst electrolysis technologies, solid oxide electrolysis cells (SOECs) have the key advantage of high hydrogen production efficiency,[2,3] such that it is predicted to have a lower cost of hydrogen than alkaline electrolysis by 2030.[4] Although long-term durability of SOECs has been a concern, significant progress has been made.[2,5–7] A major degradation issue that remains is the redistribution of nickel (Ni) in Ni-YSZ fuel electrodes during electrolysis operation. Specifically, Ni is often seen to migrate away from the Yttria Stabilized Zirconia (YSZ) electrolyte,[8–18] leading to performance degradation.[13]

Ni migration is typically attributed to a gradient in the Ni/YSZ wetting angle within the electrode active region.[12] Proposed causes include a fuel-gas composition gradient, oxygen vacancy buildup at Ni-YSZ interfaces at high electrolysis potentials, and electrowetting.[9–13,19] It has also been suggested that Ni migration results from an initial tendency of Ni particles to become isolated from the surrounding matrix.[8] The Ni transport mechanism is generally believed to be surface diffusion for typical operating temperatures of ≤800 °C,[10,13] whereas vapor phase transport *via* Ni hydroxides may be important at higher temperature. Understanding and modeling Ni migration have been challenging in part due to the divergent results. Table 1 summarizes reported life tests of Ni-YSZ-supported SOECs. Some reports show no evidence of migration[20–22] and in one case Ni migration towards the electrolyte was observed.[17] The widely varying results are probably partly due to different testing conditions,[15] with temperatures ranging from 750 to 950 °C, current densities from 0.5 to 2.0 A cm^{-2}, and steam/hydrogen partial pressure ratios from 50/50 to 90/10. It also seems likely that the different Ni migration results can be partly attributed to the different microstructural characteristics of the Ni-YSZ electrode, including Ni/YSZ/pore volume fractions, feature sizes, and three-phase boundary (TPB) density. The latter directly affects the electrode overpotential, which is believed to provide the driving force for Ni migration.[6,10,14,19] Different Ni-YSZ microstructures may facilitate or retard Ni migration. For example, Monaco *et al.* reported that a coarser cermet electrode strongly promoted Ni migration under electrolysis operation.[14]

In this paper, we test the hypothesis that the Ni/YSZ/pore volume fractions in the Ni-YSZ electrode play an important role in determining Ni migration. As shown in Table 1, which

[a]*Department of Materials Science and Engineering, Northwestern University, Evanston, Illinois, 60208, USA*
[b]*Univ. Grenoble Alpes, CEA, Liten, DTCH, 38000 Grenoble, France*
[c]*ThermoFisher Scientific, 627 00 Brno, Czech Republic*
[d]*Department of Materials Science and Engineering, University of Michigan, Ann Arbor, 48109, MI, USA*

Table 1 A summary of reported SOEC Ni migration observations. Ni depletion widths are estimated from reported SEM images. Volume fractions given are either from microscopic characterization or estimated from reported NiO and YSZ weights, and assuming that the porosity derives mainly from the shrinkage of NiO reduction to Ni, yielding a pore volume fraction equal to 40% of the Ni volume fraction.[23] These results are for Ni-YSZ-supported cells where the NiO-YSZ functional layers are sintered at high-temperature without pore formers, such that they are nearly fully dense

Ni migration direction	Depletion width [μm]	H_2O/H_2 [%/%]	Current density [A cm^{-2}]	Temperature [°C]	Time [h]	NiO [wt%]	Ni [vol%]	YSZ [vol%]	Pore [vol%]	Ref.
Away from electrolyte	7	90/10	−1.25	800	9000	~70	40	33	28	13
	3	50/50	−1.0	850	1000	55 to 60	31–34	48–53	21–23	9
	11	50/50	−0.5	800	18 000	Uncertain				10
	5	90/10	−0.5	800	1000	60 to 70	34	37	29	14
	8	90/10	−0.8	750	600	55 to 65	32	43	25	12
	1	80/20	−1.0	800	1000	65 to 70	37–40	33–38	26–28	15
	3	80/20	−1.5							
No migration	—	80/20	−0.5							
	—	60/40	−1.5							
	—	50/50	−1.0	800	1000	50	28	53	19	16
	—	50/50	−0.5	850	1300	55 to 60	31–34	48–53	21–23	17
Toward electrolyte	N/A	90/10	−2.0	950	68					

summarizes prior Ni migration results, these volume fractions vary widely and yet there is no clear correlation with Ni migration. However, such comparisons might not be expected to yield definitive results because of the variation in testing conditions and other Ni-YSZ electrode microstructural differences. In order to systematically analyze the effect of the Ni/YSZ/pore volume fractions, here we characterize the Ni distribution after SOEC life testing in Ni-YSZ made with two different NiO/YSZ weight ratios (the electrode is initially prepared as NiO-YSZ and subsequently reduced to Ni-YSZ). Values used are at either end of the typical range shown in Table 1, including 70 wt% NiO (~38 vol% Ni, 35 vol% YSZ, and 27 vol% pore in the reduced electrode) and 50 wt% NiO (~26 vol% Ni, 57 vol% YSZ, and 17 vol% pore in the reduced electrode). The microstructural and electrochemical characteristics of these two different functional layers are examined to help understand their different Ni migration results.

Experimental

Solid oxide cell geometry

Both cell types consisted of a YSZ electrolyte with Ni-YSZ electrodes on both sides, a geometry that simplifies cell fabrication, life testing, and data interpretation. The electrodes were made from different weights of NiO and YSZ with no pore former; upon exposure to a H_2-rich fuel, the NiO reduces to Ni while the associated volume reduction produces porosity. In one cell type denoted "70|70", shown in Fig. 1a, both electrodes were made using 70 wt% NiO – 30 wt% YSZ, a composition that yields sufficient porosity to provide low gas diffusion resistance.[24] The other cell type denoted "70|50/70," illustrated in Fig. 1b, was the same except for a 12 μm-thick functional layer on the SOEC side made using 50 wt% NiO – 50 wt% YSZ. The lower Ni content was used only in the functional layer because of its relatively low porosity that would yield an excessive gas diffusion resistance over the full electrode thickness.[24] During high-current SOEC operation, high gas diffusion resistance can significantly decrease the H_2O/H_2 partial pressure ratio near the electrolyte, which has been shown to decrease Ni migration.[15,25] Thus, the cell designs in Fig. 1 ensure that Ni migration is tested at the same H_2O/H_2 ratio in both cell types, providing a clear comparison of the effect of functional layer Ni content on Ni migration.

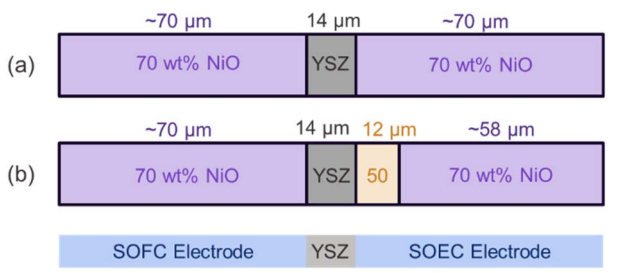

Fig. 1 Schematic cell structures of (a) "70|70" with 70 wt% NiO – 30 wt% YSZ on both sides, and (b) "70|50/70" with a 12 μm-thick 50 wt% NiO – 50 wt% YSZ functional layer on the SOEC side replacing the 70 wt% NiO – 30 wt% YSZ layer.

Cell manufacturing methods

The symmetric cells were manufactured by tape-casting NiO-YSZ electrode tapes made using the desired amounts of NiO (Fuel Cell Materials) and YSZ (Yttria Stabilized Zirconia with 8 mol% Y_2O_3, Tosoh). The YSZ electrolyte tape contained YSZ with 1 wt% Fe_2O_3 (Alfa Aesar) sintering aid. The tapes were layered to produce the structures shown in Fig. 1 and then hot pressed at 82 °C and 3 tonnes in^{-2} for 15 minutes. The laminated structure was cut into 1.5 cm × 1.5 cm green bodies. The cells were held at 600 °C for 1 hour in air to remove organic residue, then sintered at 1325 °C for 6 hours in air, with heating and cooling rates of 3 °C min^{-1}. The cells were reduced in humidified H_2 that was diluted in 97% Ar for 100 hours at 800 °C. In order to achieve flat cells with dense YSZ electrolytes by co-firing, good shrinkage matching along with full YSZ densification is required; the measures taken to achieve this for the different NiO-YSZ compositions are described elsewhere.[24]

Assuming that the NiO-YSZ layers are fully densified after sintering and that a 40% volume contraction occurs upon reducing NiO to Ni,[23] the volume fractions of the reduced electrodes are expected to be 40% Ni, 33% YSZ, and 27% porosity for the 70 wt% NiO tapes, *versus* 28% Ni, 53% YSZ, and 19% porosity for the 50 wt% NiO tapes. As will be seen below, these values are in reasonable agreement with volume fractions measured by 3D tomography.

Electrochemical characterization

The cells were precisely laser scribed into 1 cm × 1 cm squares, following the method developed by Cox[26] that avoids shorting across the thin YSZ electrolyte. Silver current collector wires (Thermo Scientific Chemicals), were double-twisted and attached to each side of the cell using silver paste (DAD-87 Shanghai Synthetic Resin Research Institute).

The life tests were done for 500 hours with −1 A cm^{-2} current density at 800 °C in 85% H_2O – 15% H_2 (gas flow rate of 200 sccm), conditions where Ni migration is typically observed in SOEC mode.[12–15] H_2 was produced using a Hydrogen G200 H_2 generator system (ProtonOnSite) and the H_2O/H_2 ratio was controlled by a vapor delivery module (Bronkhorst, VDM Series). Electrochemical testing was done with a Squidstat™ Plus (Admiral Instruments). During cell operation with current applied, one electrode of the cell operated in SOFC mode and another in SOEC mode.

Electrochemical impedance spectroscopy (EIS) was performed with an excitation amplitude of 20 mV over a frequency range of 1 MHz–100 mHz, recording 10 steps per decade, in a 4-point setup at open circuit voltage (OCV). The equivalent circuit model fitting was done using a complex nonlinear least square (CNLS) solver.[27] The quality of the fit was calculated by the residuals between experimentally measured and fitted EIS data.

Microstructural characterization

For microscopy, the cells were vacuum infiltrated in epoxy (Buehler Epothin II) to fill the pores, then mechanically polished to 50 nm alumina suspension. Scanning electron microscope (SEM) imaging was performed with a JEOL-7900 FLV using backscatter electron detection at 1 kV. To achieve good statistical accuracy of electrode phase fractions *versus* depth, SEM image data from five different randomly selected regions, each showing ∼45 μm of electrode–electrolyte interface, were combined. 3D tomography was done using a Helios 5 Hydra Plasma FIB-SEM (ThermoFisher) with through-the-lens and backscatter detectors. 3D data was smoothed, segmented, and analyzed as described by Winiarski[28] to determine Ni/YSZ/pore phase fractions, phase mean diameter, and TPB density. The size of contiguous Ni-pore interfaces is also obtained; this is important because Ni surface diffusion is expected to occur mainly on these interfaces and therefore be confined each contiguous interface. Here we introduce two Ni-pore interfacial characteristics – average projected length $\bar{l}_z$ in the z direction

$$\bar{l}_z = \frac{\sum (l_z \times A_i)}{\sum A_i}, \quad (1)$$

and average interface area $\bar{A}$

$$\bar{A} = \frac{\sum A_i}{N_c}, \quad (2)$$

where A_i is the surface area of a contiguous interface, l_z is the projected length along the direction perpendicular to the electrode–electrolyte interface, and N_c the number the clusters.

To complement the experimental data, artificial microstructures were generated using the truncated Gaussian random field model. As detailed in Moussaoui *et al.*,[29] the method has been adapted to produce representative three-dimensional (3D) Ni-YSZ electrode microstructures. The input parameters used to emulate the two experimental microstructures were the volume fractions and mean phase diameters of Ni and YSZ. The volume fractions were deduced from the NiO : YSZ weight fraction, under the assumption that the electrode is fully dense in its oxidized state. The obtained Ni and YSZ volume fractions were found to be in good agreement with those measured on the 3D reconstructions. Mean phase diameters measured on the two experimental electrode images were used as initial guesses for generating the synthetic microstructure. A loop was added on the algorithm in such a way that the mean particle size calculated on 2D slices extracted from the simulated microstructure matched the experimental ones. The mean Ni and YSZ diameters for other electrode compositions were obtained by linear extrapolation of the measured values with NiO weight fraction. The connected TPB densities and the contiguous Ni-pore interfacial areas were calculated using the tools described in Moussaoui *et al.*[30] Ni-pore interface size parameters were calculated based on eqn (1) and (2). All the microstructural parameters of the synthetic microstructure are provided in Table S1 of the SI material.

Results

Microstructural evolution

Fig. 2 shows cross sectional SEM images of the 70|70 (a) and 70|50/70 (b) cells after 500 hours life testing in 85% H_2O – 15% H_2 at 800 °C and −1 A cm^{-2}. The backscatter electron detector

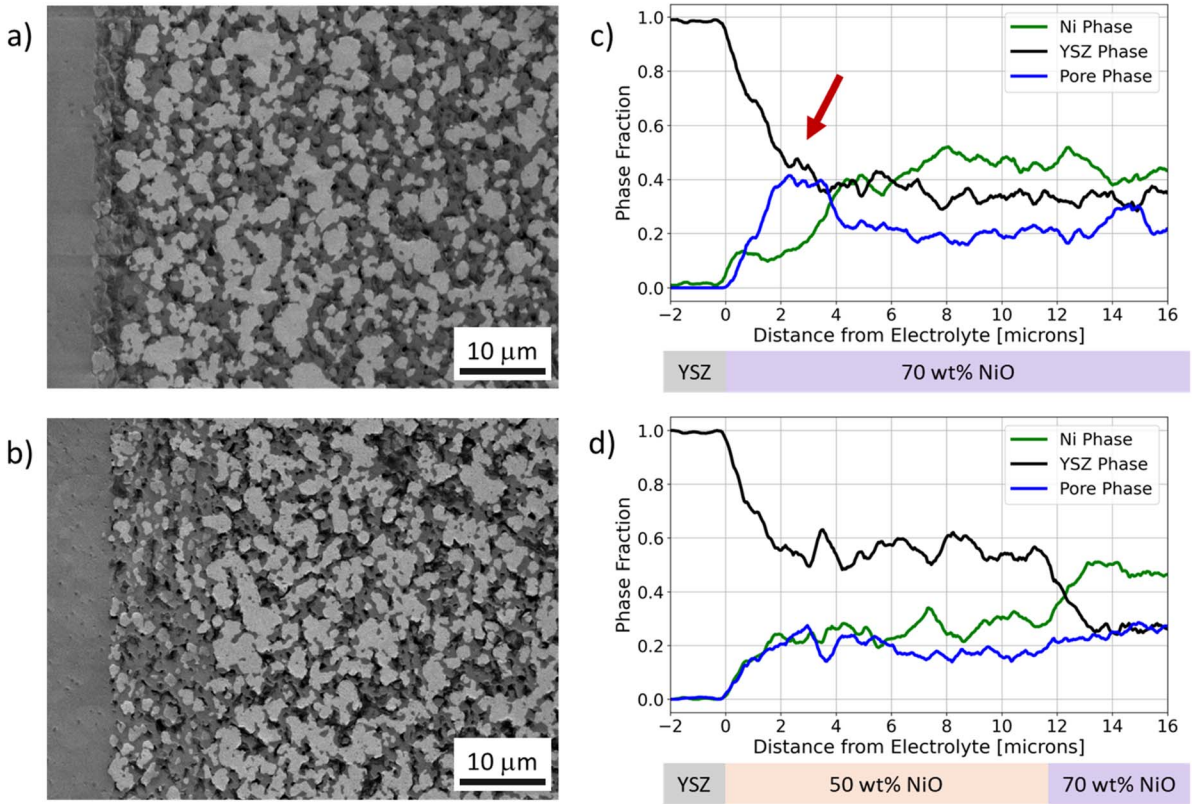

Fig. 2 Cross sectional SEM images showing the (a) 70|70 and (b) 70|50/70 cells after 500 hours life testing at −1 A cm^{-2} at 800 °C in 85% H_2O – 15% H_2. Ni has a light grey contrast, pores are black, and YSZ is a darker grey. Also shown are phase fractions *versus* distance taken from 2D image analysis for the (c) 70|70 and (d) 70|50/70 cells. Red arrow indicates Ni migrated zone.

was used to provide uniform contrasts of all Ni, connected or isolated. In Fig. 2a, Ni is clearly depleted from the region within 3–4 µm of the electrolyte. A plot of phase fractions *versus* distance (Fig. 2c), taken from 2D image analysis for the 70|70 cell, shows a clear decrease in Ni and an increase in pore fraction in this region. A baseline comparison cell from the same batch, imaged after reduction for 100 hours without cell operation, has a uniform Ni content throughout the electrode (see Fig. S1a). Thus, the Ni redistribution occurred during cell operation. Similar Ni depletion in was observed in other 70|70 cells life tested under these conditions (see Fig. S2a). Note that all the phase fraction profiles reported here have an apparent YSZ/Ni-YSZ interface broadening of ~1.5 µm that results from measuring phase fractions across interfaces that are not perfectly planar. The Ni and pore depletions vary in the same way in the interface region, showing that this is not Ni migration but rather broadening.

Fig. 2b shows a typical SEM image from the 70|50/70 cell after life testing. There is a lower density of Ni particles in the 50 wt% NiO layer, but they appear to be uniformly distributed. Fig. 2d shows the phase distributions. The 50 wt% NiO layer has a lower Ni and pore content along with higher YSZ content, in agreement with expectations based on the weights and NiO reduction. The Ni, pore, and YSZ phase fractions are reasonably constant within the functional layer; although there are small variations in the Ni and pore fractions, they appear to be the same as that observed for an identical cell before cell operation (see Fig. S1b). Even if this represents Ni migration, it is clearly much less than for the 70 wt% NiO electrode. Other life tested 70|50/70 cells show similar results with no significant Ni migration observed (see Fig. S2b).

The SOFC-side electrodes were also examined, but since they are not the focus of this report, they are included in the SI

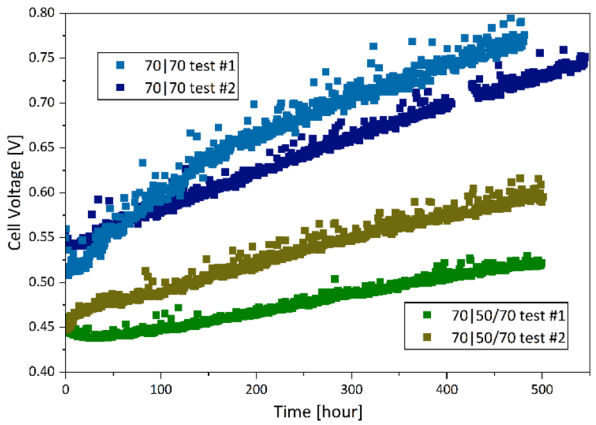

Fig. 3 Cell voltage *versus* time for two different 70|70 and 70|50/70 cells during operation at 85% H_2O – 15% H_2, 800 °C, −1 A cm^{-2} for 500 hours. There was a 20 hours current interruption in one of the 70|70 life tests due to an unplanned computer shutdown. Tests #1 and #2 represent different samples from repeated experiments.

document. No evidence of Ni redistribution was observed after life testing (see Fig. S3). This agrees with many prior reports where little to no Ni migration was observed in SOFC operation.[9]

Electrochemical degradation

Fig. 3 shows the cell voltage *versus* time for the 70|70 (a) and 70|50/70 (b) cells during operation at 85% H_2O – 15% H_2, 800 °C, −1 A cm^{-2} for ∼500 hours. The initial voltage is ∼20% lower for the 70|50/70 cell. The voltage increases approximately linearly with time in all cases, after some initial variations over the first ∼100 hours. The degradation rate is lower, 0.2 to 0.28 mV h^{-1}, for the 70|50/70 cells *versus* 0.4 mV h^{-1} for the 70|70 cells. These results indicate a substantially lower resistance and lower degradation rate for Ni-YSZ electrode made with 50 wt% NiO *versus* 70 wt% NiO.

Fig. 4 shows EIS spectra taken from the two cell types prior to and after life testing. Comparison of the "before test" spectra show a much smaller electrode polarization resistance, consistent with the lower initial cell voltage in Fig. 3. After testing, the electrode polarization responses increase for both cells, and the ohmic response increases significantly for the 70|70 cell. Fits to the data are shown, based on an equivalent circuit model (see Fig. S4) that includes in series an electrolyte resistance, an inductance associated with test setup wiring, a Warburg gas diffusion element, a transmission line model (TLM) element, and a high frequency response. This is the same as prior Ni-YSZ models,[31] except for the latter response that is included to fit the high frequency feature seen in some of the data. The transmission line model represents the charge transfer process at three phase boundaries (TPBs) in concert with ionic transport in the Ni-YSZ electrode.

Fig. 5 summarizes the resistance values for each impedance response from the fits. First, we focus on the ohmic and polarization resistances of the cells before and after operation (Fig. 5a). The initial ohmic resistances are the same, but increase more after cell operation for the 70|70 cell. As reported previously,[15] this is a key indicator of Ni migration resulting from the Ni-depleted zone of porous YSZ becoming part of a thicker electrolyte. As noted above, the initial polarization resistance is much smaller for the 70|50/70 cell. An increase in

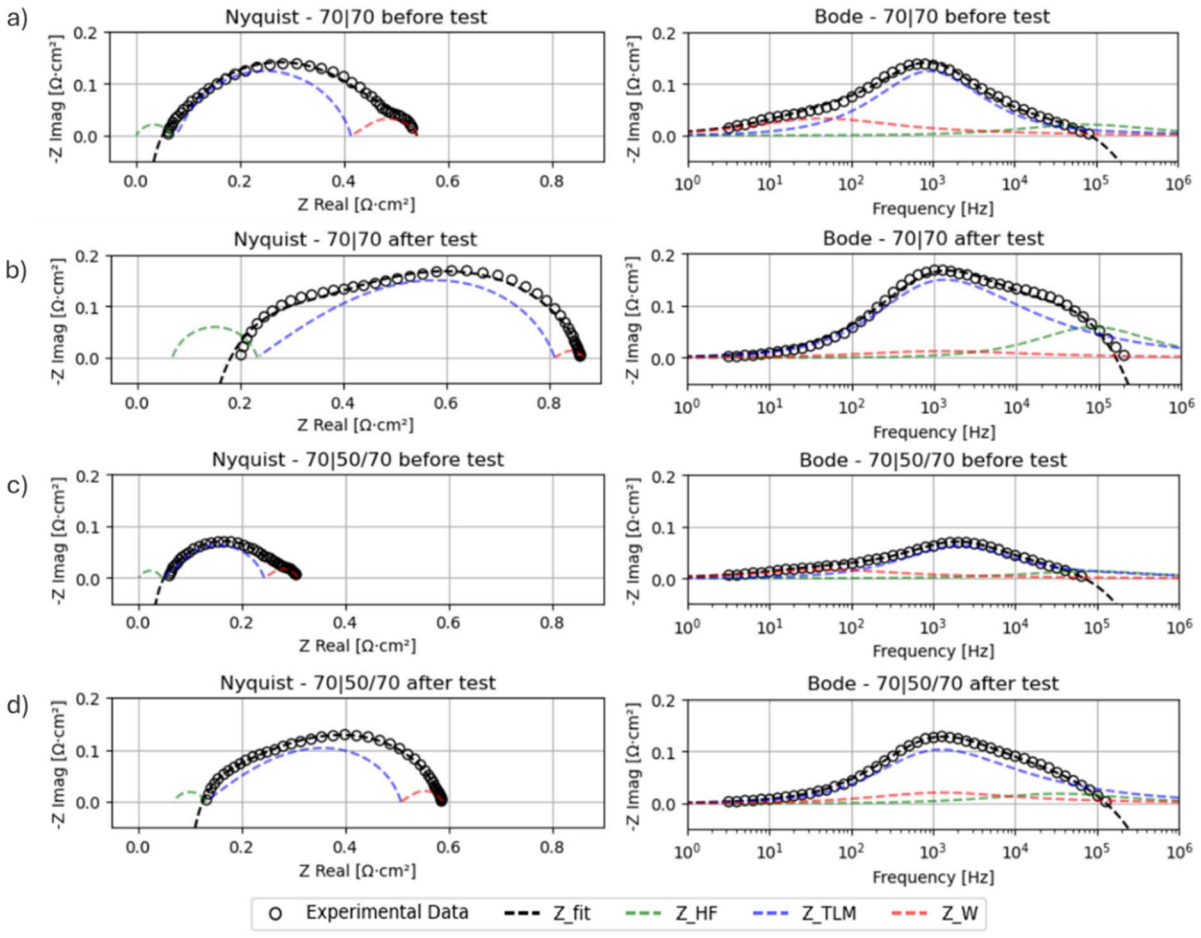

Fig. 4 Nyquist and Bode plot measured at 800 °C and 85% H_2O – 15% H_2 from (a and b) 70|70 and (c and d) 70|50/70 cells (both from tests #2 in Fig. 3) (a and c) are measured before as pristine cells (b and d) are measured after SOEC operation at 85% H_2O – 15% H_2, 800 °C, −1 A cm^{-2} for 500 hours. Also, shown are fits to the experimental data using an equivalent circuit model consisting of electrolyte resistor, inductance, Warburg gas diffusion element (Z_W), a transmission line model element (Z_{TLM}), and a high frequency resistance (Z_{HF}). The inductance, not highlighted, is responsible for the positive excursion of Z_{imag} at high frequency.

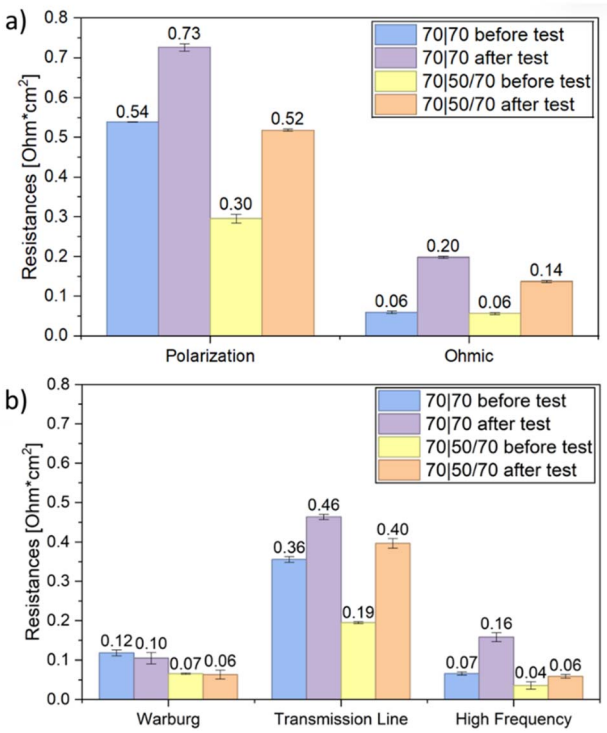

Fig. 5 Resistances of 70|70 and 70|50/70 cells before and after cell operation at 85% H_2O – 15% H_2, 800 °C, −1 A cm^{-2} for 500 hours, derived from the EIS fitting. Ohmic and polarization resistances are shown in (a), while (b) breaks down the polarization components. Error bars are based on fitting sensitivity analysis.

the polarization resistance is seen in both cells and is presumably the result of early-stage break-in and Ni coarsening that is often seen in Ni-YSZ-based cells.[17,25,32]

Fig. 5b breaks the fitting results down further. The TLM resistance is the dominant part of the electrode polarization, and is initially much lower for the 70|50/70 cell. This can be explained by a lower resistance on the 50 wt% NiO (SOEC-side) electrode of the 70|50/70 cell, as seen in prior EIS measurements of symmetric Ni-YSZ cells with these compositions.[24] The increase in TLM resistance after life testing is actually somewhat larger for the 70|50/70 cell; this may be due to an increased tendency for Ni and pores to become isolated for low Ni/pore volume fractions, resulting in reduced connected TPB density.[9] The Warburg resistance values are small for both cells due to the reasonably high porosity of Ni-YSZ made with 70 wt% NiO, and any changes after life testing are generally small compared to measurement errors. The high frequency resistance only becomes significant after life testing the 70|70 cell. Noting that high frequency responses are typically associated with interfaces, a possible explanation is an increased grain boundary resistance in the electrolyte due to void formation.[33]

Discussion

In the following discussions, we examine possible reasons for the difference in Ni migration observations for the two different Ni-YSZ compositions, including the electrochemical characteristics and electrode microstructure.

Electrochemical characteristics

Ni-YSZ electrochemical characteristics are important because Ni migration is driven by the overpotential gradient across the electrode functional region,[6,8,14,15,34,35] which is mainly dependent on the TLM resistance. Fig. 4 and 5 indicate a lower TLM resistance for the 50 vol% NiO electrode. Thus, the absence of Ni migration in this lower Ni electrode (Fig. 2) can be explained at least in part by a lower overpotential gradient, as driving force for Ni migration.[14,34] Reported EIS measurements of Ni-YSZ electrodes *versus* Ni content show a TLM resistance that decreases with decreasing NiO wt% from 70 to 50,[24,36] suggesting that there should be a continuous decrease in Ni migration with decreasing Ni content in Ni-YSZ electrodes.

Electrode microstructure

Ni evolution in a Ni-YSZ microstructure is constrained by the YSZ phase, and hence is dependent on the specific microstructure including Ni, pore, and YSZ volume fractions. For

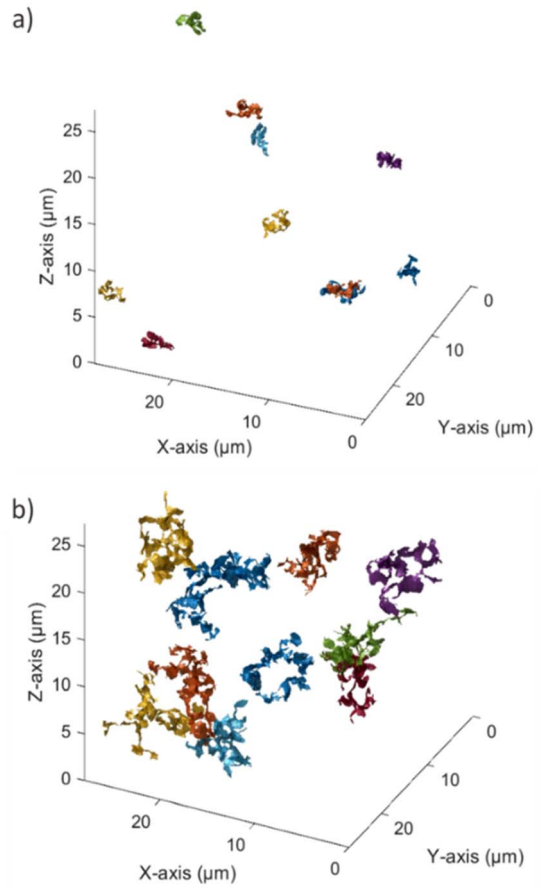

Fig. 6 3D volume of Ni-pore interfaces of (a) 50 wt% NiO and (b) 70 wt% NiO electrodes. For clarity, only the 10 largest interfaces are shown with each isolated Ni-pore interface indicated by a different color. For more plots, see Fig. S6.

Table 2 Measured 3D data from the Ni-YSZ electrodes including phase volume fractions, three phase boundary densities, and Ni-pore interface characteristics. The latter includes surface-area weighted average Ni-pore surface areas $\bar{A}$ and "z-lengths" $\bar{l}_z$ (see eqn (1) and (2)). Maximum z-lengths along with maximum and total surface areas are also given

NiO–YSZ (initial wt%)	Volume fraction [%]			TPB density [μm^{-2}]	z-length [μm]		Surface area [μm^2]		
	Ni	YSZ	Pore		Average	Max	Average	Max	Total
50-50	25.6	57.0	17.4	2.44	0.97	3.52	0.80	20.03	16 310
70-30	37.5	34.9	27.6	2.54	2.43	10.50	1.75	127.30	20 400

example, high-temperature Ni coarsening in Ni-YSZ electrodes was much slower for lower Ni content (initial NiO : YSZ weight ratio of 50 : 50 *versus* 65 : 35).[32] It was argued that decreasing NiO wt% both reduces pore volume and increases YSZ volume, thereby limiting the space available for Ni movement, increasingly confining the Ni phase. Here we discuss a related aspect – how Ni content affects the extent of Ni-pore interfaces in the microstructure. As noted earlier, these are important because Ni surface diffusion is believed to occur on these interfaces.[13]

The Ni-pore interfaces in Ni-YSZ electrodes made with 50 and 70 wt% NiO were examined in FIB-SEM-measured 3D microstructures with size 27 × 28 × 27 μm^3 (see Fig. S5). Fig. 6 shows the Ni-pore interfaces in the microstructures – only the largest ten interfaces are shown for clarity. Table 2 summarizes the Ni-pore interface characteristics, along with phase volume fractions and TPB densities. The low Ni content electrode (Fig. 6a) has isolated Ni-pore interfaces that are relatively small, *i.e.*, with projected z-length $\bar{l}_z < 1$ μm and area $\bar{A} < 1$ μm^2 (see Ni-pore interface size distribution in Table S2). These interfaces are too small to allow Ni surface diffusion over the observed Ni depletion width of 3–4 μm (Fig. 2). The higher Ni content electrode (Fig. 6b) has larger average and maximum Ni-pore interface z-length along with a larger average, maximum, and total interface areas, including many with z-length ≥10 μm, providing a network for long-range Ni migration. Note that lower NiO content decreases Ni-pore interface content because both Ni and pore volume fractions decrease. Overall, the lower NiO content should substantially suppress Ni migration, as observed in Fig. 2.

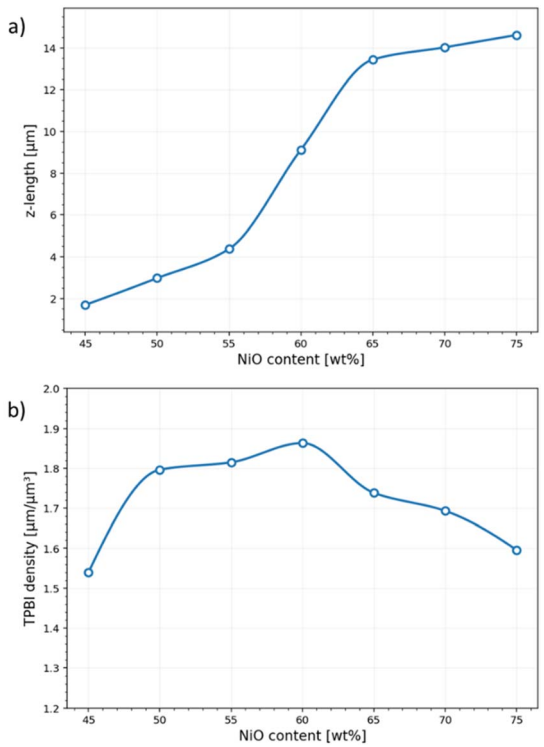

Fig. 7 Evolution of the average z-length of Ni-pore interfaces (a) and TPB density (b) as a function of the NiO content. Microstructural properties were calculated on 3D artificial microstructures (15 μm^3 cubes) generated for two Ni and YSZ particle sizes: dNi = 0.8 μm and dYSZ = 0.72 μm (for the 50 wt% NiO layer of the 70|50/70 cell), and dNi = 1 μm and dYSZ = 0.69 μm (for the 70 wt% NiO layer of the 70|70 cell).

Table 2 also shows that the active TPB densities in the two electrodes are almost identical. This is consistent with the lower TLM resistance of the cell with the 50 wt% NiO electrode because the higher YSZ content increases ionic transport. This can be estimated using a standard TLM model in the thick-electrode limit where $R_{TLM} \cong \sqrt{R_{LS}/\sigma_{ion}\rho_{TPB}}$.[37] Here, ρ_{TPB} is the TPB density, R_{LS} is the TPB line-specific resistance (10 000–30 000 Ω cm at 800 °C),[38] and σ_{ion} is the ionic conductivity of the YSZ phase in the electrode given by the YSZ conductivity (0.01 S cm^{-1} at 800 °C) multiplied by the YSZ volume fraction (see Table 2) divided by the YSZ phase tortuosity (estimated to be 1.03 for 50 wt% NiO and 1.12 for 70 wt% NiO). Using R_{LS} = 20 000 Ω cm, this yields $R_{TLM} \approx 0.24$ Ω cm^2 for 50 wt% NiO and 0.32 Ω cm^2 for 70 wt% NiO. This shows the same trend as the measured TLM resistances in Fig. 5; the absolute values are in good agreement considering uncertainties in the input values, especially R_{LS}. These factors also affect the width δ of the electrode active region across which the potential gradient is present. This active depth is given by $\delta \cong \sqrt{R_{LS}\sigma_{ion}/\rho_{TPB}}$ in the transmission line model, yielding 6.7 μm for 50 wt% NiO and 4.9 μm for 70 wt% NiO using the above-mentioned values. Note that the latter thickness agrees with the observed Ni depletion depth of ~4 μm (Fig. 2c). The larger δ for the 50 wt% NiO electrode combines with its lower overpotential (noted above) to yield an overall weaker overpotential gradient, decreasing the driving force for Ni migration.

Artificial electrode microstructures

To further investigate Ni-pore interfaces over a wider range of NiO : YSZ weight fractions, artificial 3D microstructures were generated. Fig. 7a shows that the average z-length l_z exhibits a sharp increase as NiO wt% increases from 55 to 65%, in

agreement with the large difference in z-lengths between the 50 and 70 wt% electrodes observed experimentally (Table 2). The results indicate that below ~55–60 wt% NiO, Ni diffusion should be limited to very short distances within the electrode, whereas above this range the microstructure allows diffusion over a distance larger than observed Ni depletion width. Fig. 7b shows that the TPB density ρ_{TPB} has a maximum near 60 wt% NiO, similar to prior reports.[30,36] ρ_{TPB} for 50 wt% NiO is similar to that for 70 wt% NiO, in agreement with the experimental values in Table 2. As noted above, the comparable ρ_{TPB} combines with the higher effective ionic conductivity due to higher YSZ content in the 50 wt% NiO functional layer to yield a lower transmission-line resistance and larger active layer depth;[39] these combine to reduce the overpotential gradient driving Ni migration. Although the trends in the simulated l_z and ρ_{TPB} agree well with the experimental results, the absolute values differ; this is attributed to differences in particle size distributions, which exhibit greater variability in real microstructures and are difficult to reproduce in synthetic microstructures.[29]

Summary and conclusions

In this study, Ni-YSZ electrodes with 70 wt% and 50 wt% initial NiO content were tested under identical conditions, demonstrating for the first time that Ni migration is essentially eliminated for the lower NiO content. The results of electrochemical and microstructural characterization suggest two mechanisms that can explain this compositional effect. First, the transmission line resistance was substantially lower for the lower NiO content, resulting in reduced electrode overpotential. Combined with a larger electrode active region for the lower NiO content, this yields a substantially reduced overpotential gradient, reducing the gradient in Ni wetting angle that is believed to drive Ni migration. Second, Ni-pore interfaces – believed to be the primary pathways for Ni transport by surface diffusion – were isolated for the lower Ni content electrodes, with length substantially less than the observed Ni migration length. In contrast, the high NiO electrode had Ni-pore interface widths larger than observed Ni migration lengths, providing continuous pathways for Ni surface diffusion.

The experimental results are augmented by synthetic microstructure modeling over a wider range of electrode NiO contents (45–75 wt%). The results confirm large changes in Ni-pore interface length with NiO content, revealing a percolation threshold near 55–60 wt% NiO where Ni-pore interface lengths increase dramatically. Below this threshold, migration is inherently limited by the availability of diffusion pathways regardless of electrochemical conditions, while above it, migration is possible but depends on electrochemical operating conditions.

This study provides clear design principles for improving Ni-YSZ electrode durability, with significant practical implications. Ni-YSZ fuel electrodes are often fabricated with high NiO contents of ~70 wt% NiO, with the advantage that they provide high electronic conductivity. While this works well in solid oxide fuel cell (SOFC) applications where Ni migration is typically not observed, they appear to be poorly suited for industrial SOEC systems where multi-year stable operation is necessary for economical and energy-efficient renewable hydrogen/fuel production. Ni-YSZ electrodes made with ~50 wt% NiO provide superior long-term stability while delivering sufficient electronic conductivity. This Ni-YSZ composition adjustment represents a straightforward pathway to enhanced stability without requiring significant changes in SOEC materials or fabrication processes.

Finally, this work establishes a general framework for understanding how electrode composition affects the microstructural and electrochemical characteristics that control degradation. The principles identified here—reducing driving force through lower resistance and limiting transport pathway through microstructural design—may extend beyond Ni migration to other degradation mechanisms such as particle coarsening and to a broader range of electrochemical cells.

Author contributions

All authors contributed to the work presented in this paper. Conceptualization P. P., P. V., K. T., J. L., S. B.; data curation P. P., H. D., B. W.; formal analysis P. P, H. D., M. H., J. L., S. B.; funding acquisition S. B.; investigation P. P., H. D., B. W.; methodology P. P, S. B; project administration S. B.; supervision J. L., S. B.; validation P. P, J. L., S. B.; visualization P. P., H. D.; writing – original draft P. P, S. B; writing – review & editing P. P, H. D., M. H., K. T., J. L., S. B.

Conflicts of interest

There are no conflicts to declare.

Data availability

The data supporting this article has been included as part of supplementary information (SI) and repository data sharing. Supplementary information: additional figures and tables supporting the main text. See DOI: https://doi.org/10.1039/d6ta01398h.

Repository data sharing: experimental and artificial 3D microstructures of different Ni-YSZ electrode composition; see DOI: https://doi.org/10.21985/n2-0byw-q887.

The data supporting the findings of this study are available from the corresponding authors upon reasonable request.

Acknowledgements

The authors gratefully acknowledge financial support by the U.S. Department of Energy, National Energy Technology Laboratory (Award Number P010317777) and Basic Energy Sciences (Award Number DE-SC0016965). This work made use of the NUFAB facility (RRID:SCR_017779) and EPIC facilities of Northwestern University's NUANCE Center, which has received support from the SHyNE Resource (NSF ECCS-2025633), the IIN, and Northwestern's MRSEC program (NSF DMR-2308691). This work also made use of the MatCI Facility (RRID:SCR_017947)

which receives support from the MRSEC Program (NSF DMR-2308691) of the Materials Research Center at Northwestern University.

References

1 E. Larson, *Net-zero America: Potential Pathways, Infrastructure, and Impacts*, Princeton University, 2020.
2 A. Hauch, R. Kungas, P. Blennow, A. B. Hansen, J. B. Hansen, B. V. Mathiesen and M. B. Mogensen, *Science*, 2020, **370**, 6118.
3 S. H. Jensen, C. Graves, M. Mogensen, C. Wendel, R. Braun, G. Hughes, Z. Gao and S. A. Barnett, *Energy Environ. Sci.*, 2015, **8**, 2471–2479.
4 H. Nami, O. B. Rizvandi, C. Chatzichristodoulou, P. V. Hendriksen and H. L. Frandsen, *Energy Convers. Manage.*, 2022, **269**, 116162.
5 Y. Wang, W. Li, L. Ma, W. Li and X. Liu, *J. Mater. Sci. Technol.*, 2020, **55**, 35–55.
6 S. J. McPhail, S. Frangini, J. Laurencin, E. Effori, A. Abaza, A. K. Padinjarethil, A. Hagen, A. Leon, A. Brisse, D. Vladikova, B. Burdin, F. R. Bianchi, B. Bosio, P. Piccardo, R. Spotorno, H. Uchida, P. Polverino, E. A. Adinolfi, F. Postiglione, J. H. Lee, H. Moussaoui and J. Van Herle, *Electrochem. Sci. Adv.*, 2022, **2**, e2100024.
7 B.-K. Park, Q. Zhang, P. W. Voorhees and S. A. Barnett, *Energy Environ. Sci.*, 2019, **12**, 3053–3062.
8 M. B. Mogensen, M. Chen, H. L. Frandsen, C. Graves, A. Hauch, P. V. Hendriksen, T. Jacobsen, S. H. Jensen, T. L. Skafte and X. Sun, *Fuel Cells*, 2021, **21**(5), 415–429.
9 M. Trini, A. Hauch, S. De Angelis, X. Tong, P. V. Hendriksen and M. Chen, *J. Power Sources*, 2020, **450**, 227599.
10 C. E. Frey, Q. P. Fang, D. Sebold, L. Blum and N. H. Menzler, *J. Electrochem. Soc.*, 2018, **165**, F357–F364.
11 L. Rorato, Y. Shang, S. Yang, M. Hubert, K. Couturier, L. Zhang, J. Vulliet, M. Chen and J. Laurencin, *J. Electrochem. Soc.*, 2023, **170**, 034504.
12 A. Nakajo, G. Rinaldi, P. Caliandro, G. Jeanmonod, L. Navratilova, M. Cantoni and J. Van Herle, *J. Electrochem. Energy Convers. Storage*, 2020, **17**, 041004.
13 M. B. Mogensen, A. Hauch, X. Sun, M. Chen, Y. Tao, S. D. Ebbesen, K. V. Hansen and P. V. Hendriksen, *Fuel Cells*, 2017, **17**, 434–441.
14 F. Monaco, M. Hubert, J. Vulliet, J. P. Ouweltjes, D. Montinaro, P. Cloetens, P. Piccardo, F. Lefebvre-Joud and J. Laurencin, *J. Electrochem. Soc.*, 2019, **166**, F1229–F1242.
15 M. P. Hoerlein, M. Riegraf, R. Costa, G. Schiller and K. A. Friedrich, *Electrochim. Acta*, 2018, **276**, 162–175.
16 D. Cox and S. A. Barnett, *ECS Trans.*, 2023, **111**, 915–923.
17 A. Hauch, S. D. Ebbesen, S. H. Jensen and M. Mogensen, *J. Electrochem. Soc.*, 2008, **155**, B1184–B1193.
18 Y. Wang, C. R. Wu, B. F. Zu, M. F. Han, Q. Du, M. Ni and K. Jiao, *J. Power Sources*, 2021, **516**, 230660.
19 Z. Jiao, E. P. Busso and N. Shikazono, *J. Electrochem. Soc.*, 2020, **167**, 024516.
20 Q. Liu, Q. Zhang, P. W. Voorhees and S. A. Barnett, *J. Phys.: Energy*, 2020, **2**, 014006.
21 L. Le, C. Coyle, L. Seymour, J. Zaengle, J. Escobar, T. Liu, J. Bao, K. Meinhardt and O. A. Marina, *Electrochem Solid St*, 2023, **MA2023–01**, 150.
22 O. A. Marina, L. Le, C. Coyle, R. Springer, S. Karki and T. Liu, *Electrochem Solid St*, 2024, **MA2024–01**, 2251.
23 S. D. Angelis, P. S. Jørgensen, E. H. R. Tsai, M. Holler, G. Fevola and J. R. Bowen, *Mater. Charact.*, 2020, **162**, 110183.
24 P. Pibulchinda and S. A. Barnett, in preparation.
25 A. Hauch, S. Pylypko, G. Cubizolles and J. Mouginn, *ECS Trans.*, 2021, **103**, 437.
26 D. M. Cox and S. A. Barnett, *J. Electrochem. Soc.*, 2023, **170**, 024514.
27 J. Grimes and S. A. Barnett, *J. Electrochem. Soc.*, 2021, **168**, 084514.
28 B. Winiarski, P. Barthelemy, C. Jiao, D. Laeveren, D. Cox and S. A. Barnett, *Microsc. Microanal.*, 2024, **30**, 305–306.
29 H. Moussaoui, J. Laurencin, Y. Gavet, G. Delette, M. Hubert, P. Cloetens, T. Le Bihan and J. Debayle, *Comput. Mater. Sci.*, 2018, **143**, 262–276.
30 H. Moussaoui, R. K. Sharma, J. Debayle, Y. Gavet, G. Delette and J. Laurencin, *J. Power Sources*, 2019, **412**, 736–748.
31 B.-K. Park, R. Scipioni, D. Cox and S. A. Barnett, *J. Mater. Chem. A*, 2020, **8**, 4099.
32 Y.-C. K. Chen-Wiegart, D. Kennouche, J. S. Cronin, S. A. Barnett and J. Wang, *Appl. Phys. Lett.*, 2016, **108**, 083903.
33 F. Tietz, D. Sebold, A. Brisse and J. Schefold, *J. Power Sources*, 2013, **223**, 129–135.
34 A. Nakajo, G. Rinaldi, P. Caliandro, G. Jeanmonod, L. Navratilova, M. Cantoni and J. Van herle, *J. Electrochem. Energy Convers. Storage*, 2020, **17**, 041004.
35 Z. Jiao, E. P. Busso and N. Shikazono, *J. Electrochem. Soc.*, 2020, **167**, 024516.
36 J. R. Wilson and S. A. Barnett, *Electrochem. Solid-State Lett.*, 2008, **11**, B181–B185.
37 S. Zhang, H. Wang, t. yang, M. Y. Lu, C. Li, C. Li and S. Barnett, *J. Mater. Chem. A*, 2020, **8**, 25867–25879.
38 Z. Gao, L. V. Mogni, E. C. Miller, J. G. Railsback and S. A. Barnett, *Energy Environ. Sci.*, 2016, **9**, 1602–1644.
39 B.-K. Park, D. Cox and S. A. Barnett, *Nano Lett.*, 2021, **21**(19), 8363–8369.